Journal of Power Sources 396 (2018) 297–303

Contents lists available at ScienceDirect

Journal of Power Sources

journal homepage: www.elsevier.com/locate/jpowsour

An advanced Na-$NiCl_2$ battery using bi-layer (dense/micro-porous) β″-alumina solid-state electrolytes

Keeyoung Jung[a,1], Hee-Jung Chang[b,1], Jeffery F. Bonnett[b], Nathan L. Canfield[b], Vincent L. Sprenkle[b], Guosheng Li[b,*]

[a] Materials Research Division, Research Institute of Industrial Science & Technology, Pohang, South Korea
[b] Electrochemical Materials & Systems Group, Energy Processes & Materials Division, Pacific Northwest National Laboratory, Richland, WA, 99352, USA

HIGHLIGHTS

- Bi-layer (porous/dense) solid state electrolyte.
- Infusion of molten Na through pore voids in the porous layer.
- Lower battery over potentials.
- High energy efficiency.

GRAPHICAL ABSTRACT

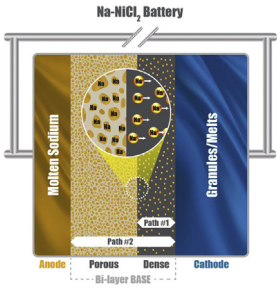

ARTICLE INFO

Keywords:
Stationary energy storage
Na battery
Solid-state electrolyte
Na-metal halide battery
Bi-layer composite

ABSTRACT

Sodium metal halide (Na-MH) batteries present tremendous opportunities for grid scale energy storage applications. In this work, we describe an advanced Na-MH battery operating at 190 °C using a bi-layer (thin dense/thick porous layers) β″-alumina solid-state electrolyte (BASE). The novel design of the bi-layer BASE promotes high Na-ion transportation by reducing the Na^+ ion path length. The excellent battery performances are achieved with a stable capacity retention of 350 W h/kg up to > 350 cycles (~6 months). Moreover, owing to the thin dense layer of BASE, the round trip energy efficiency (or discharging energy density) of the tested battery shows an ~8% increase compared to that of state of the art Na-MH battery reported in the literature. Results from this work clearly demonstrate that advanced Na-MH batteries using bi-layer BASEs can have significant impacts on improving battery performances at lower operating temperatures, and further stretch its feasibility in stationary energy storage applications.

1. Introduction

With the rapidly increasing electricity production from renewable resources such as wind power and photovoltaic cells, demands of low-cost, long-cycle (service) life, safe, and reliable large-scale energy storage are stimulating great interests in design of new battery materials, safety/reliability enhancement of battery systems, and practical demonstrations of advanced battery technologies [1–3]. Over the years, lithium-ion batteries (LIB) have been widely deployed as a suitable energy storage technology for portable electronic devices and electric powered vehicles owing to its high energy density. Along with the success of commercial LIBs, LIB technologies have been also chosen for most large-scale energy storage demonstrations. However, despite their applicability and production capability, concerns about battery safety,

* Corresponding author.
E-mail address: guosheng.li@pnnl.gov (G. Li).
[1] K. Jung and H.J. Chang are equally contributed to this work.

https://doi.org/10.1016/j.jpowsour.2018.06.039
Received 12 April 2018; Received in revised form 5 June 2018; Accepted 10 June 2018
0378-7753/ Published by Elsevier B.V.

rapidly rising cost of raw materials, limited cycle life, and etc., still remain as challenges for current LIBs technology [4,5]. Therefore, developing next-generation battery technologies is critical, especially for long-duration (> 4 h) energy storage system to fuel the continuous growth of the renewable energy sector and improve the reliability of the grid [6].

Of particular interest, sodium (Na)-based batteries are attractive candidates for large-scale energy storage applications because Na is much cheaper and more abundant than lithium. In fact, high-temperature Na β″-alumina batteries (NBB) with high energy densities, such as Na-S and Na-metal halide batteries (Na-MH or ZEBRA), have been extensively investigated and demonstrated in the past [7–15]. However, technical roadblocks to the use of traditional NBBs, (e.g., intrinsic materials degradation, complicated cell assembly requirements, high manufacturing cost, the safety concerns associated with Na-S batteries, etc.) prohibit further market penetration in large-scale energy storage applications [16–18].

Recently, our research has been focusing on mitigating challenges associated with high-temperature NBBs by lowering the operating temperature [16,19]. We have reported several key investigations of intermediate-temperature (IT) Na-MH batteries operated at 190 °C, which is nearly 100 °C below the operating temperature (280 – 320 °C) of conventional Na-MH batteries. The IT Na-MH batteries exhibit a stable cycling performance for over 1000 cycles with excellent capacity retention while fast degradation occurs in high-temperature (280 °C) Na-MH batteries. The better capacity retention at lower operating temperatures was attributed to slower particle growth (suppressed Oswald ripening process) in cathode materials [19]. Another important advantage from the lower temperature battery operations is the implementation of cost-effective sealing technologies that can employ conventional high temperature polymers, such as polyethylene and fluorinated polymers, replacing the complicated and high cost sealing methods required for conventional high temperature Na-MH systems [20].

While the lower operating temperature of Na-MH batteries is beneficial in terms of longer cell cycle life and simpler cell architecture, battery performance inevitably could be affected. Specifically, the Na ion conductivity of the β″-alumina solid-state electrolyte (BASE) strongly depends on the operating temperature, and ohmic resistance of the BASE increases as the operating temperature decreases [21]. Simply reducing the thickness of the BASE might be one of the solutions to circumvent this technical challenge, however its robustness can be drastically decreased by lowering its mechanical strength. In previous work, we have reported the fabrication of a bi-layer BASE for reducing the resistance of the BASE [22]. The initial design of the bi-layer BASE (shown in Fig. 1) was inspired by the multi-layer tape-casting method typically used to fabricate the anode of solid oxide fuel cells (SOFC) [23,24]. Similar to the porous anode of a SOFC that allows hydrogen gas to be diffused through, we modified the BASE by casting a porous layer with micro-porosities facing the molten sodium anode of a planar Na-MH battery (colored in orange, Fig. 1). In the porous structure, the transportation of molten sodium (colored in orange, Fig. 1) can be facilitated through the pore voids resulting in reducing the overall resistance of the BASE because the electric resistivity of molten sodium in the porous layer is much lower than the resistivity of the BASE. In other words, the Na^+ ion transportation occurs mainly by taking a shorter path length (path #1 shown in Fig. 1). Our previous report of the bi-layer BASEs were mainly focused on investigation of the mechanical properties and the process optimization, electrochemical evaluations have not been made on bi-layer BASEs.

In this work, we present the first successful realization of a high-energy-efficiency intermediate-temperature Na-MH battery operating at 190 °C and using bi-layer BASEs that consist of a thin dense layer and a relatively thicker porous layer. We demonstrate that by reducing the path length of solid-state electrolytes, IT Na-MH batteries have excellent roundtrip efficiency that is up to 8% higher than cells using thick dense BASEs. Our battery also exhibits ~100% capacity retention after > 350 cycles. Finally, through electrochemical and spectroscopic characterizations, we document superior robustness and reliable performance of our bi-layer BASEs for grid-scale energy storage applications.

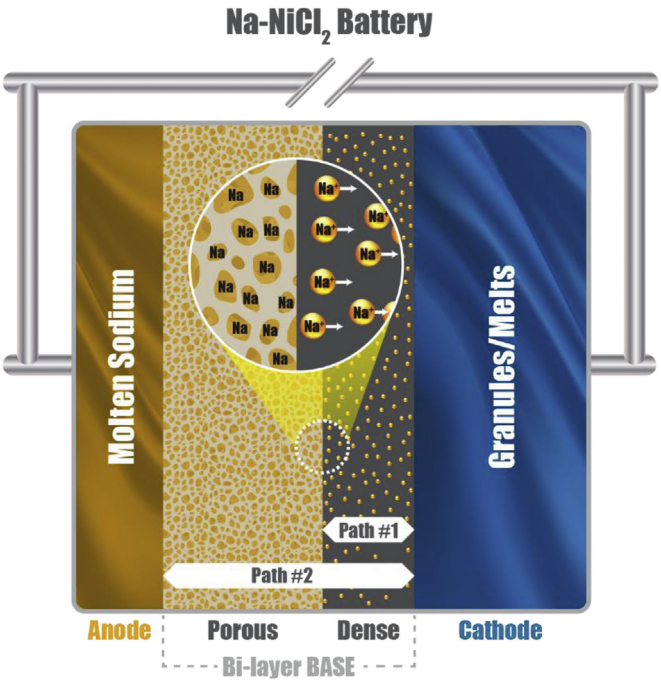

Fig. 1. A schematic view of the Na-$NiCl_2$ battery with bi-layer BASE. Bi-layer BASE consists of dense and porous layers. Majority of Na^+ ion transportation happens through the dense layer with a short path length (path #1) instead of path #2 with a longer path length.

2. Experimental procedures

Since most of the experimental processes including cathode preparation, melts synthesis, BASE fabrication process, and cell assembly, have been mentioned in our previous publications [19,22,30], only brief descriptions of these processes are given in here.

Double layer β″-alumina solid-state electrolyte (BASE) fabrication. Fig. S1 shows a schematic flow chart for fabricating double-layer BASE in the lab. Similar to the process mentioned in previous publications, BASE discs used in this work were fabricated by converting α-alumina/yttria-stabilized zirconia (α-Al_2O_3/YSZ) composite discs through a vapor phase process. Briefly, 60 vol%, high purity α-Al_2O_3 (> 99.8%) and 40 vol% YSZ (5 mol% Y_2O_3) powders were mixed by high energy attrition milling in isopropanol to obtain fine particle size powders. Two slurries, one for the dense layer and the other for the porous layer, were made from the powders by mixing with organic solvent and additives (dispersant, binder, and plasticizer) using low-energy ball milling. The only difference between two slurries is that graphite powder (SLC1512P, ~12 μm, 15%) were added into the slurry for making pores in the porous layer. Two slurries were cast into two type sheets (~125 μm thickness), sheet_D and sheet_P, using a tape caster (step 1 in Fig. S1) for making dense and porous layers, respectively. Then, obtained two different sheets were laminated and laser cut into a desired thickness and size (step 2 in Fig. S1). Three different BASEs, a double-layer BASE with 125 μm dense and 250 μm porous layers (D125/P250), a double-layer BASE with 250 μm dense and 250 porous layers (D250/P250), and a BASE with 500 μm dense layer only (D500), were fabricated and tested in this work. For instance, D125/P250 was made by laminating one sheet_D and two sheet_Ps together. Similarly, two sheet_Ds and two sheet_Ps were laminated together for

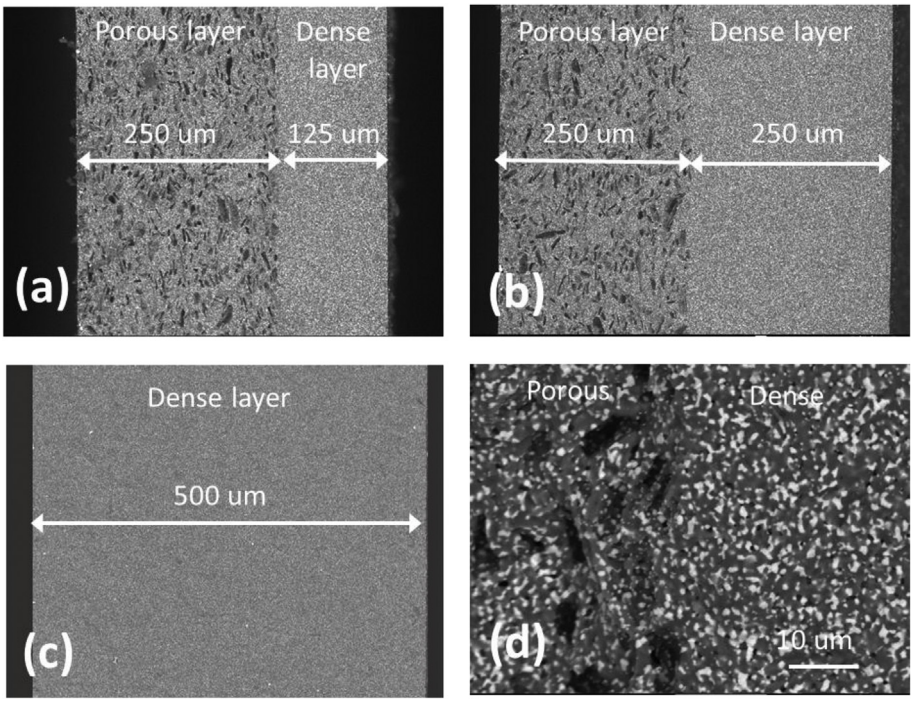

Fig. 2. SEM images. Back scattering images for fracture surfaces of double-layer BASEs with different thickness for the dense layer. (a) D125/P250, x300; (b) D250/P250, x300; (c) D500, x300; (d) high magnification image for the interface between the porous and dense layer, x2500. Bright spots shown in SEM images are YSZ particles.

making D250/P250, and four sheet_Ds were used for D500. Then the discs were fired at 1600 °C in air to obtain fully sintered α-Al_2O_3/YSZ discs (step 3 in Fig. S1, burning out graphite powders and sintering). Finally (step 4 in Fig. S1), the sintered α-Al_2O_3/YSZ discs were buried in conversion powders ($NaAlO_2$/β″-Al_2O_3) and heat treated at 1450 °C in air to convert α-Al_2O_3 into β"-Al_2O_3. The conversion occurs by simultaneous transport of sodium cations and oxygen anions from the conversion powders to the α-Al_2O_3/YSZ discs.

Cathode materials preparation. Ni Cathode used in here consist of 62.2 wt% Ni (Novamet, Type 255), 34.2 wt% NaCl (Alfa Aesar, 99.99%), and 3.6 wt% additives (FeS, aluminum, NaI, and NaF, Sigma Aldrich). The cathode powders were thoroughly mixed using a low-energy ball milling in a nitrogen environment. Then, well-mixed cathode powders were turned into granules using a granulator (Freund TF-Labo). Sodium tetrachloroaluminate ($NaAlCl_4$), the melts, was prepared by a high temperature reaction (up to 320 °C) using NaCl (10% excessive amount) and $AlCl_3$ powders in a glove box.

Battery assembly and cell cycling. As shown in Fig. S2, a planar type cell configuration (button cell) consists of end-caps (stainless steel), a α-alumina fixture, a BASE (3 cm^2 active area), cathode materials, anode shim, and polymer seals, etc. First, the dense side (cathode side) of a double-layer BASE disc was glass-sealed to the α-alumina fixture, and the porous layer (anode side) of the BASE disc was pretreated with saturated lead acetate (Pb $[CH_3COO]_2$) aqueous solution followed by a heat treatment at 400 °C. The fixture was then transferred into a glove box for the cell assembly. Second, 1 g of cathode granules was added to the cathode side of the fixture and 0.7 g of melt was vacuum infiltrated into the granules at an elevated temperature of 200 °C. Finally, the fixture was enclosed with end caps using polymer seals. Assembled cells were moved from the glove box to temperature controlled furnaces, and cell tests were conducted in air. For the conditioning cycle, the cells were cycled between cutoff voltages of 2.8 V (charge limit) and 1.8 V (discharge limit) at lower currents up to 10 mA. For different current test, the charge current was fixed to 20 mA and the discharge currents vary from 20, 30, 60, 90, 120, and 150 mA. Long-term cycling for the D125/P250 cell was done with charging and discharging currents at 20 and 30 mA, respectively. All cell cycling tests were conducted using an Arbin potentiostat (MSTAT 8000).

Electrochemical Impedance Spectroscopy (EIS). EIS measurements were performed for Sodium (Na)-symmetric cells in the glove box. Two main differences between a Na-symmetric cell and a button cell are (1) metallic Na was added to the cathode and anode sides of Na-symmetric cell, (2) Al metal O-rings were used for Na-symmetric cells. EIS measurements were conducted at different cell temperatures (300, 250, 200, and 150 °C) after holding the designated cell temperature for an hour. An Electrochemical Interface Spectrometer (Solartron 1287) and an Impedance/Gain-Phase Analyzer (Solartron 1260) were used to collect impedance spectra, and the swiping frequency range of the impedance measurement is between 100 kHz and 0.1 Hz.

X-ray Diffraction (XRD): The fabricated BASEs were monitored by XRD analysis using a Rigaku MiniFlex II table-top instrument.

Scanning electron microscopy (SEM): To determine the morphology of the cathode materials, the fracture surface of the cathode was analyzed by SEM. The cells (D125/P250) after long-term cycling test were disassembled in the glove box, and its cathodes were quickly transferred to the SEM chamber to minimize exposure to air. A JEOL JSM-7001 F field emission and JEOL 5900 SEM with silicon drift detector were used for collecting images at back-scattering mode. An Oxford energy-dispersive X-ray (EDX) spectroscopy analysis was used for collecting element maps.

3. Results and discussion

As mentioned in the Experimental section, three different BASEs were fabricated, and their fracture surfaces were analyzed using scanning electron microscopy (SEM) to determine the bi-layer structures, dense layer (D) and porous layer (P). The cross-section image of D125/P250 is shown in Fig. 2a (backscatter image). The dense layer (~125 μm, right side) and the porous layer (~250 μm, left side) are clearly observed. SEM images for D250/P250 and D500 are shown in Fig. 2b and c, respectively. Fig. 2d shows a higher magnification image of the interface between porous and dense layers. The average size of voids in the porous layer is slightly larger than 10 μm, which is near the particle size (~12 μm) of graphite powders added to the slurry as scarifying pore formers. The XRD spectra for the dense and porous sides were shown in Fig. S3, and they both are in good agreement with characteristic peak patterns of the BASE reported in the literature.

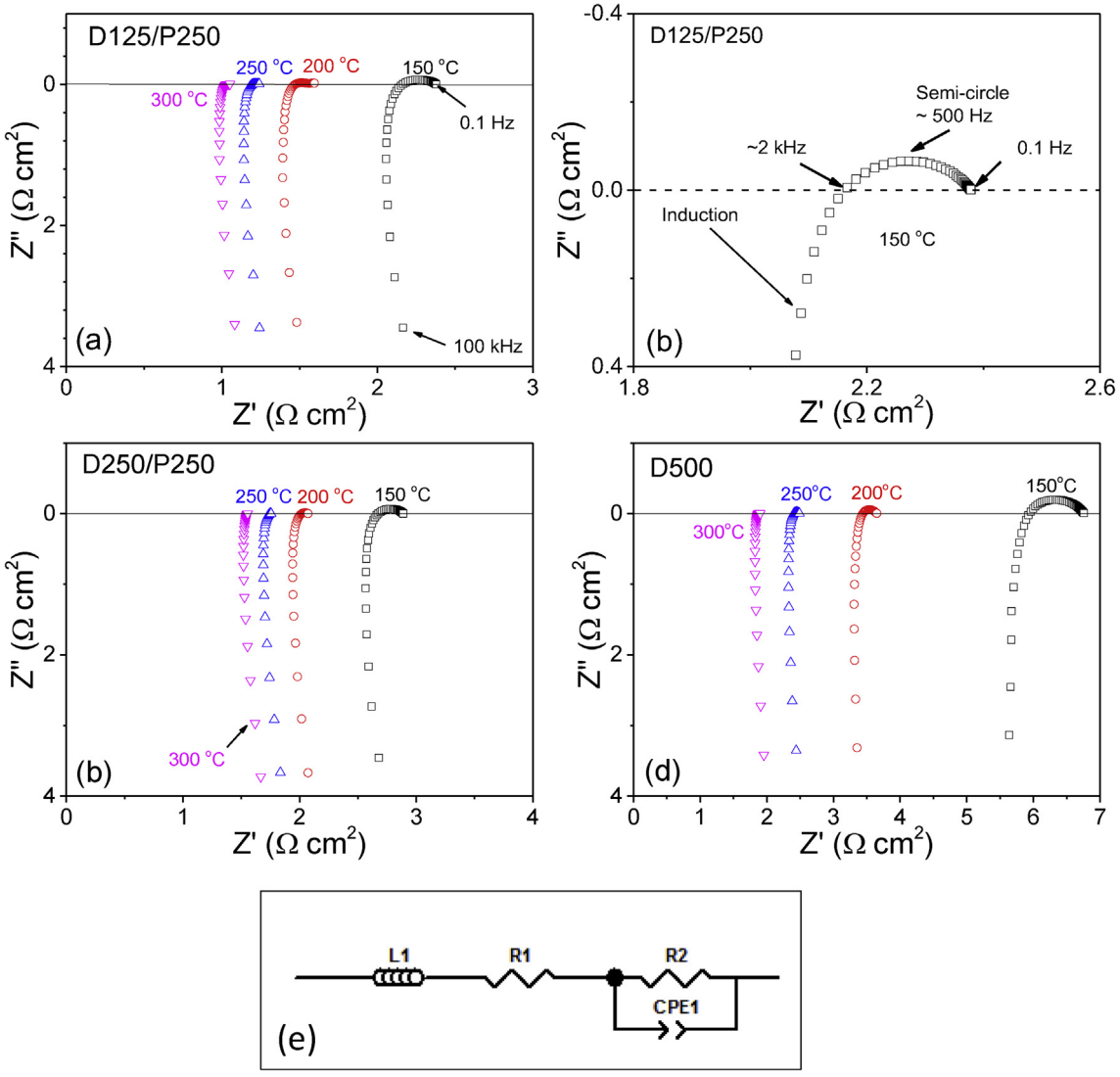

Fig. 3. Impedance spectra of BASEs with different layer thickness. (a) D125/D250, (b) An enlarged view for the semi-circle of D125/P250 at 150 °C, (c) D250/P250, (d) D500, and (e) A model circuit for fitting impedance spectra. Impedance measurements were performed for four different temperatures at 150 °C (black), 200 °C (red), 250 °C (blue), and 300 °C (magenta), respectively. Please note that Nyquist plots are intentionally given in different scales for Z″(y-axis) and Z′ (x-axis) to show semi-circles in a better way. (For interpretation of the references to color in this figure legend, the reader is referred to the Web version of this article.)

First, we conducted electrochemical impedance spectroscopy (EIS) measurements on Na-symmetric cells with three different BASEs (D125/P250, D250/P250, and D500) at the elevating temperatures from 150 to 300 °C. The frequency swiping range of the EIS measurements was 100 kHz to 0.1 Hz. The detailed EIS plots are shown in Fig. 3a for D125/P250, Fig. 3c for D250/P250, and Fig. 3d for D500, respectively. As shown in Fig. 3b (an enlarged view of the impedance plot of D125/P250 at 150 °C), a typical impedance plot consists of a rapidly rising induction period in the high-frequency region (> 2 kHz), and that is followed by a semi-circle (~500 Hz). Because the symmetric cells have molten sodium on both sides of BASEs, in principle, it should show following impedance components: (1) the bulk and grain boundary resistance of BASE, (2) the charge transfer resistance at the BASE/molten sodium interface, and (3) the bulk resistance of molten sodium. Among those resistances, the bulk resistance of molten sodium is negligible from the fitting because it is much smaller than the other two resistances. The impedance of bulk and grain boundary resistances from the BASE tends to appear at high frequency regions (> 10 kHz), and apparently would not give complete semi-circles because of overlapping with the induction at high frequency regions [25]. The observed representative frequency of the semi-circle (~500 Hz) generally agrees with the behaviors relating to the charge transfer reported in the literature [26,27]. It is also interesting to see that the semi-circle becomes smaller at higher temperatures. Indeed, this observation is an important evidence for the assignment above because the higher temperature can improve the Na wetting on the BASE and promote faster charge transfer at the interface. Finally, a model circuit employed for fitting impedance plots is shown in Fig. 3e. It consists of L_1 (inductance), R_1 (ohmic resistance), R_2 (charge transfer resistance), and CPE_1 (a constant phase element). In general, CPE_1 is required to obtain a good fit for a slightly depressed semi-circle of the impedance plot, and those depressions typically originate from various factors, including the inhomogeneity of the BASE surface.

R_1 values obtained from fitting results are plotted in Fig. 4a as a function of the thickness of the dense BASEs and temperatures. As mentioned above, R_1 represents the overall ohmic resistance of the BASE, because other ohmic resistances are negligible for the Na-symmetric cells studied in here. Fig. 4b shows the temperature dependence of the R_1 for different BASEs. Arrhenius-type behavior was clearly observed for all plots. An overall activation energy (E_{a1}) for bulk Na-ion transportation in the BASE is calculated from their slopes. The E_{a1} of D500 is about 0.19 ev, which is quite similar to values reported in the

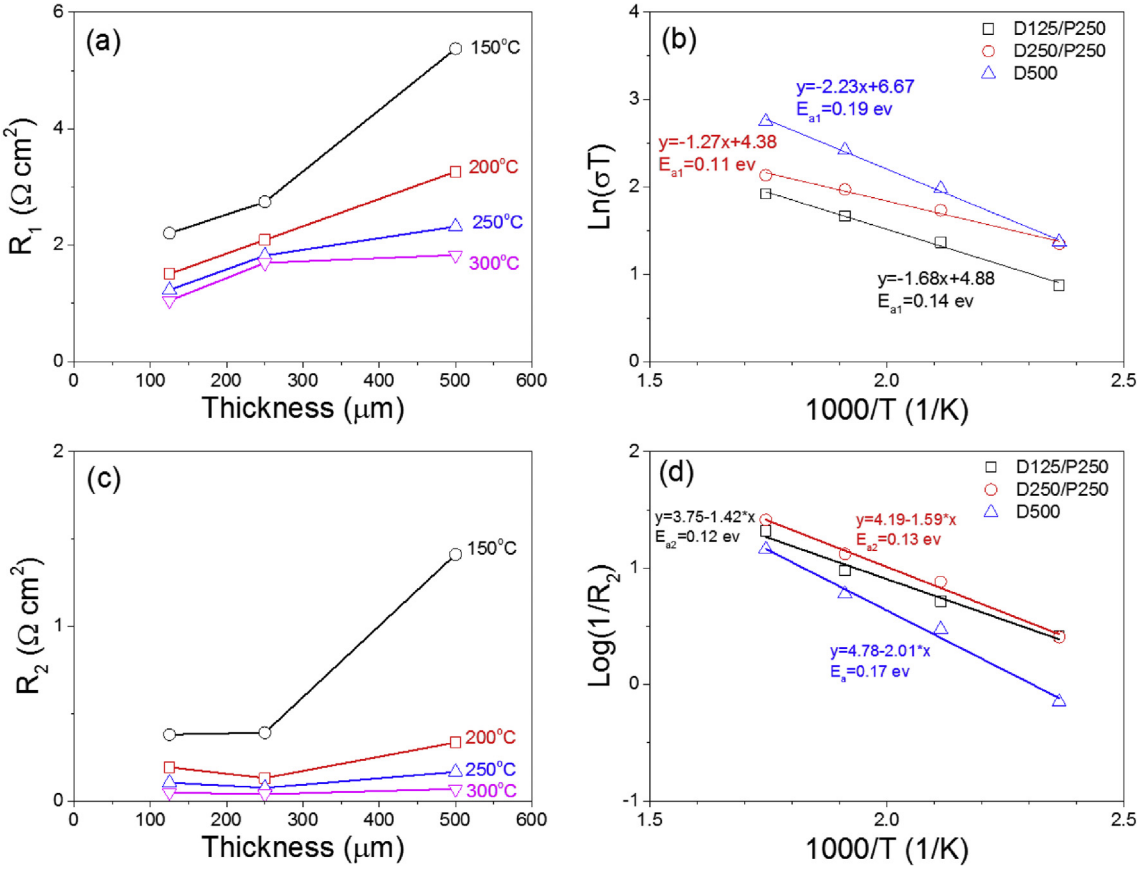

Fig. 4. Analysis for impedance spectra. (a) Plots for R_1 (ohmic resistance) (b) Temperature dependent Arrhenius plots for R_1, and activation energies (E_{a1}) were calculated for each BASE; (c) Plots for R_2 (charge transfer); (d) Temperature dependent (Arrhenius type) plots for R_2, and activation energies (E_{a2}).

literature [28,29]. However, we found that the calculated activation energies of bi-layer BASEs tend to be smaller than that of BASE with a dense layer only (D500). In our work, we cautiously attribute this discrepancy to imperfections in the bi-layer BASE. In an ideal situation, the transport of Na ions should take place mainly through the dense layer of the bi-layer BASE because molten Na can reach the dense layer by physically occupying pores of the porous layer. Thus, the majority of R_1 should be close to the bulk resistance of the dense layer under the assumption that the dense layer is a main Na-ion transport pathway. However, it is possible that some pores in the porous layer are closed pores, which prevent molten Na from reaching the interface of the dense layer. This is supported by SEM and EDX mapping images (Fig. S4), in which two voids are observed in the porous layer. First type voids are filled with the molten sodium and provides a good Na path to the interface (porous/dense) and the other voids are empty (no Na). A consequence of the imperfect bi-layer BASE gives a longer path length for Na-ion transport through the BASE, which leads to deviations in calculating the activation energy for bi-layer BASEs. Despite their imperfections, the bi-layer BASEs (D125/P250 and D250/P250) show significantly reduced R_1 values compared to the R_1 value of D500. For example, the measured R_1 value for D125/P250 is ~60% smaller than that of D500 at 200 °C.

Fig. 4c shows a temperature dependence of Na-ion transport resistance (R_2) at the interfaces between the BASE and the molten Na. The rapid decrease in R_2 at the higher temperatures above 200 °C is a good evidence of excellent sodium wetting on the BASEs in either shapes. Overall, bi-layer BASEs have smaller charge transfer R_2 values compared to the D500. As the only difference between the bi-layer BASEs and the D500 BASE is the porous layer, we believe the porous interface is responsible for the smaller interfacial charge transfer resistance. Arrhenius-type fittings (Fig. 4d) were also made from R_2 plots (Fig. 4c) and the activation energies for the interfacial Na^+ ion charge transfer also were calculated. The activation energy (E_{a2} = 0.17 ev) of D500 is slightly larger than that (E_{a2} = 0.12 ev) of bi-layer BASEs. According to the literature, the activation energies for Na^+ ion charge transfer resistance at the interface between BASEs and organic electrolytes at ~50 °C are typically 0.31–0.35 ev, which are much larger than the value observed in our work [25]. Although a quantitative comparison may not be accurate due to different experimental conditions and ion-transfer mechanisms, a favorable reaction dynamic of Na^+ ion transfer exists for the interface between molten Na and the BASE.

To investigate the effect of the different BASEs on cell performances, we conducted rate capability tests for the cells with D125/P250 and D500 BASEs. Each cell was cycled with discharging currents of 20, 30, 60, 90, 120, and 150 mA (50 mA/cm^2, ~1C), and the charging current was 20 mA at 190 °C. The detailed voltage profiles of the cells with D125/P250 and D500 are shown in Fig. 5a and b, respectively. Apparently, the cell with the D500 BASE shows a much higher over-potential compared to the cell with a bi-layer BASE (D125/P250). Quantitative comparisons for voltages at the beginning of discharge (BOD) and at 50% SOC (discharge) are also shown in Fig. 5c. The plots of the discharge voltage at BOD and at 50% SOC for both cells shows continuous decrease with ascending of the discharging current. The overall energy efficiency of batteries operated at different discharge currents are also calculated and plotted in Fig. 5d. Overall, the energy efficiency of the D125/P250 cell is much higher than the D500 cell. For example, the energy efficiency of the D125/P250 cell is 89% at a discharging current of 150 mA, however, the energy efficiency of the D500 cell is only 81% at the same discharging current.

Finally, we performed long-term cycling tests for cells with the bi-layer BASE (D125/P250) to evaluate its long-term stability for energy storage applications. D125/P250 cells were cycled at the charge current

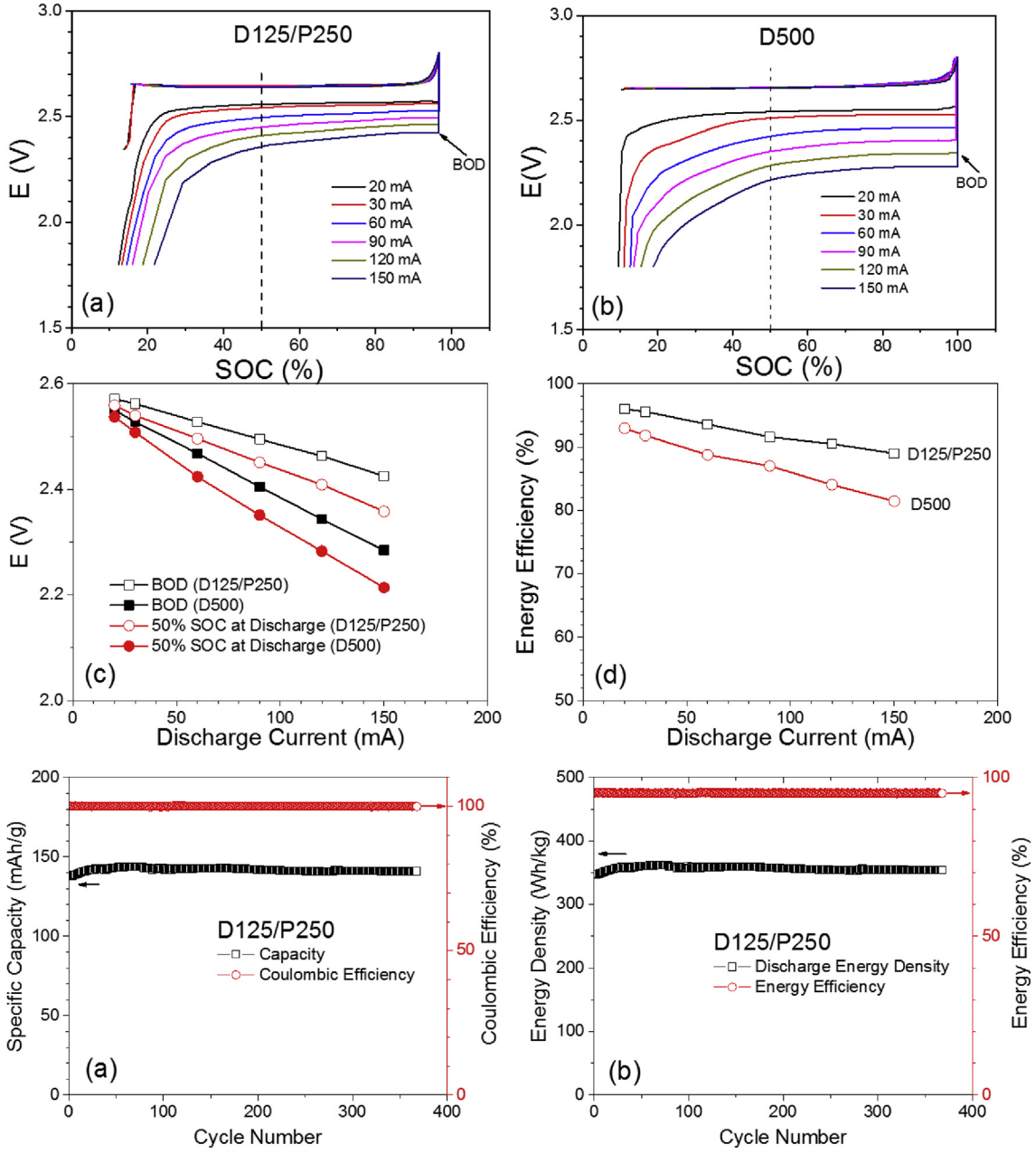

Fig. 5. Voltage profiles for the cells with different discharging currents (20–150 mA). (a) D125/P250, (b) D500. BOD represents the voltage at the beginning of discharge. The dash lines indicate the 50% state of charge (SOC). The charging current is 20 mA for all measurements. (c) The discharge voltage vs discharge current plots at BOD and 50% SOC at discharge. (d) Energy efficiency plot for D125/P250 and D500 BASEs, respectively. (e) Long-term cycling test (> 350 cycles) for D125/P250 cells. Specific capacity and Coulombic efficiency. (f) Corresponding energy density (discharge) and roundtrip energy efficiency.

of 20 mA and the discharge current of 30 mA at 190 °C over 350 cycles (~6 months). As shown in Fig. 5e, the D125/P250 cells have a specific capacity of ~138 mA h/g at the beginning of the test, reach 143 mA h/g at around 70th cycle, and then maintains a capacity of 141 mA h/g for the rest of 200 cycles. No significant particle growth was observed for Ni (1–2 μm) and NaCl (~30 μm) particles in the cathode retrieved from the D125/P250 cell after 200 cycles (SEM images and EDX mappings can be found in Fig. S5) and this observation is in a good agreement with its stable cell cycling shown above. Because of using the Na^+ ion conducting BASE, high Coulombic efficiencies (100%) are observed throughout the long-term test. Similar to the trend of the specific capacity plot, the energy density of D125/P250 cells also remains stable with high energy density of 355 W h/kg for 350 cycles (Fig. 5e). The measured roundtrip efficiency of D125/P250 cells is as high as 96% (Fig. 5f), which is ~5% higher than the energy efficiency of D250 cells operated under the same conditions (Fig. 5d).

Here, we want discuss how employing bi-layer BASEs in Na-MH batteries can greatly improve overall cell performance and reduce materials cost. The first benefit of higher roundtrip efficiency is energy saving. For example, it is possible to save up to 8% of the charging electricity for every kWh (discharging) delivered by the energy storage using bi-layer BASEs. If the total amount of electricity across the life cycle of the energy storage system is considered, the 8% charging electricity savings could result in an enormous cost reduction for the battery operation. The second benefit is reducing the materials cost ($/kW) for the battery system. If one assumes two Na-MH battery systems having the same specific capacity density, the battery using bi-layer BASE is capable of giving a higher output power since the discharging voltage loss of the cells using bi-layer BASE will be much smaller than that of using regular BASEs. Therefore, the higher energy

efficiency can be directly projected to the materials saving of the battery. As shown in Fig. 5d, the energy efficiency of the D500 cell is 91% (the discharging current at 30 mA), which indicates 9% of the total electricity is released through thermal energy. In contrast, the D125/P250 cell has a higher energy efficiency of 96%, which translates to a 4% total electricity loss as the heat release. Clearly, compared to the D500 cell, bi-layer cells could generate up to 56% less ohmic heat during the battery cycling; therefore, the third benefit of using bi-layer BASEs is more homogeneous temperature distribution in the unit cell as well as the module due to the less ohmic heat generation. Eventually, we expect the temperature management of a module consist of cells using bi-layer BASEs will be much simpler.

4. Conclusion

In summary, we have demonstrated an advanced Na-MH batteries that employs bi-layer BASEs and exhibits excellent roundtrip energy efficiency and long-term cycle life. When compared to conventional Na-MH batteries, cells with bi-layer BASEs can significantly improve energy efficiency (up to 8%). Along with the demonstrated advantages of higher discharge power, lower materials cost, and easier thermal management, we believe that advanced Na-MH batteries using BASEs with a bi-layer architecture present a compelling solution for lower operation and materials cost for large scale energy storage applications.

Declaration of interests

The authors declare no competing financial interests.

Acknowledgements

The authors are grateful to the U.S. Department of Energy Office of Electricity Delivery and Energy Reliability (Contract No. 70247) and the International Collaborative Energy Technology R&D Program (No. 20158510050010) of the Korea Institute of Energy Technology Evaluation and Planning funded by the Ministry of Trade, Industry, and Energy and POSCO, the Republic of Korea, for funding this work. Pacific Northwest National Laboratory is a multiprogram laboratory operated by Battelle Memorial Institute for DOE under Contract DE-AC05-76RL01830.

Appendix A. Supplementary data

Supplementary data related to this article can be found at http://dx.doi.org/10.1016/j.jpowsour.2018.06.039.

References

[1] Z.G. Yang, J.L. Zhang, M.C.W. Kintner-Meyer, X.C. Lu, D.W. Choi, J.P. Lemmon, J. Liu, Electrochemical energy storage for green grid, Chem. Rev. 111 (2011) 3577–3613.
[2] B. Dunn, H. Kamath, J.M. Tarascon, Electrical energy storage for the grid: a battery of choices, Science 334 (2011) 928–935.
[3] G.L. Soloveichik, Battery technologies for large-scale stationary energy storage, Annu. Rev. Cell Biol. 2 (2011) 503–527.
[4] J.W. Choi, D. Aurbach, Promise and reality of post-lithium-ion batteries with high energy densities, Nat Rev Mater 1 (2016) 16013.
[5] M.M. Thackeray, C. Wolverton, E.D. Isaacs, Electrical energy storage for transportation-approaching the limits of, and going beyond, lithium-ion batteries, Energy Environ. Sci. 5 (2012) 7854–7863.
[6] B. Battke, T.S. Schmidt, D. Grosspietsch, V.H. Hoffmann, A review and probabilistic model of lifecycle costs of stationary batteries in multiple applications, Renew. Sustain. Energy Rev. 25 (2013) 240–250.
[7] X.C. Lu, J.P. Lemmon, V. Sprenkle, Z.G. Yang, Sodium-beta alumina batteries: status and challenges, Jom-Us 62 (2010) 31–36.
[8] K.B. Hueso, M. Armand, T. Rojo, High temperature sodium batteries: status, challenges and future trends, Energy Environ. Sci. 6 (2013) 734–749.
[9] S. Ha, J.K. Kim, A. Choi, Y. Kim, K.T. Lee, Sodium-metal halide and sodium-air batteries, ChemPhysChem 15 (2014) 1971–1982.
[10] B.L. Ellis, L.F. Nazar, Sodium and sodium-ion energy storage batteries, Curr Opin Solid St M 16 (2012) 168–177.
[11] X.C. Lu, G.S. Li, J.Y. Kim, J.P. Lemmon, V.L. Sprenkle, Z.G. Yang, A novel low-cost sodium-zinc chloride battery, Energy Environ. Sci. 6 (2013) 1837–1843.
[12] E. Gerovasili, J.F. May, D.U. Sauer, Experimental evaluation of the performance of the sodium metal chloride battery below usual operating temperatures, J. Power Sources 251 (2014) 137–144.
[13] G.S. Li, X.C. Lu, J.Y. Kim, V.V. Viswanathan, K.D. Meinhardt, M.H. Engelhard, V.L. Sprenkle, An advanced Na-Fecl2 zebra battery for stationary energy storage application, Adv Energy Mater 5 (2015) 1500357.
[14] X. Ao, Z.Y. Wen, Y.Y. Hu, T. Wu, X.W. Wu, Q.M. He, Enhanced cycle performance of a Na/Nicl2 battery based on Ni particles encapsulated with Ni3s2 layer, J. Power Sources 340 (2017) 411–418.
[15] T. Wu, S.P. Zhang, X. Ao, X.W. Wu, J.H. Yang, Z.Y. Wen, Enhanced stability performance of nickel nanowire with 3d conducting network for planar sodium-nickel chloride batteries, J. Power Sources 360 (2017) 345–352.
[16] X.C. Lu, G.L. Li, J.Y. Kim, J.P. Lemmon, V. Sprenkle, Z.G. Yang, The effects of temperature on the electrochemical performance of sodium–nickel chloride batteries, J. Power Sources 215 (2012) 288–295.
[17] G.S. Li, X.C. Lu, J.Y. Kim, J.P. Lemmon, V.L. Sprenkle, Cell degradation of a Na–Nicl2 (zebra) battery, J. Mater. Chem. 1 (2013) 14935–14942.
[18] Z.Y. Wen, Y.Y. Hu, X.W. Wu, J.D. Han, Z.H. Gu, Main challenges for high performance nas battery: materials and interfaces, Adv. Funct. Mater. 23 (2013) 1005–1018.
[19] G.S. Li, X.C. Lu, J.Y. Kim, K.D. Meinhardt, H.J. Chang, N.L. Canfield, V.L. Sprenkle, Advanced intermediate temperature sodium-nickel chloride batteries with ultra-high energy density, Nat. Commun. 7 (2016) 10683.
[20] H.J. Chang, X.C. Lu, J.F. Bonnett, N.L. Canfield, S. Son, Y.C. Park, K. Jung, V.L. Sprenkle, G.S. Li, Development of intermediate temperature sodium nickel chloride rechargeable batteries using conventional polymer sealing technologies, J. Power Sources 348 (2017) 150–157.
[21] X.C. Lu, G.S. Li, J.Y. Kim, K.D. Meinhardt, V.L. Sprenkle, Enhanced sintering of beta"-Al2o3/ysz with the sintering aids of Tio2 and Mno2, J. Power Sources 295 (2015) 167–174.
[22] J.Y. Kim, N.L. Canfield, J.F. Bonnett, V.L. Sprenkle, K. Jung, I. Hong, A duplex B'-Al2o3 solid electrolyte consisting of a thin dense layer and a porous substrate, Solid State Ionics 278 (2015) 192–197.
[23] N.Q. Minh, Ceramic fuel-cells, J. Am. Ceram. Soc. 76 (1993) 563–588.
[24] D. Simwonis, H. Thulen, F.J. Dias, A. Naoumidis, D. Stover, Properties of Ni/Ysz porous cermets for sofc anode substrates prepared by tape casting and coat-mix (R) process, J. Mater. Process. Technol. 93 (1999) 107–111.
[25] F. Sagane, T. Abe, Z. Ogumi, Sodium-ion transfer at the interface between ceramic and organic electrolytes, J. Power Sources 195 (2010) 7466–7470.
[26] G.C. Farrington, Interfacial Na+ transport in beta alumina propylene carbonate system, J. Electrochem. Soc. 123 (1976) 591–595.
[27] K. Ahlbrecht, C. Bucharsky, M. Holzapfel, J. Tubke, M.J. Hoffmann, Investigation of the wetting behavior of Na and Na alloys on uncoated and coated Na-Beta"-Alumina at temperatures below 150 a degrees C, Ionics 23 (2017) 1319–1327.
[28] G.E. Youngblood, G.R. Miller, R.S. Gordon, Relative effects of phase conversion and grain-size on sodium ion conduction in polycrystalline, lithia-stabilized beta'-alumina, J. Am. Ceram. Soc. 61 (1978) 86–87.
[29] J.L. Briant, G.C. Farrington, Ionic-conductivity in Na+, K+, and Ag+ beta-'-alumina, J. Solid State Chem. 33 (1980) 385–390.
[30] H.J. Chang, N.L. Canfield, K. Jung, V.L. Sprenkle, G.S. Li, Advanced Na-Nicl2 battery using nickel-coated graphite with core shell microarchitecture, Acs Appl Mater Inter 9 (2017) 11609–11614.